frontiers in Materials

ORIGINAL RESEARCH
published: 06 July 2021
doi: 10.3389/fmats.2021.692273

A Liquid-Metal-Based Freestanding Triboelectric Generator for Low-Frequency and Multidirectional Vibration

Huaxia Deng, Zizheng Zhao, Chong Jiao, Jingchang Ye, Shiyu Zhao, Mengchao Ma and Xiang Zhong*

School of Instrument Science and Opto-electronics Engineering, Hefei University of Technology, Hefei, China

There are a lot of vibrational energies, which are low frequency, multidirectional, and broadband, in the nature. This creates difficulties for devices that aim at harvesting vibration energy. Here, we present a liquid-metal-based freestanding triboelectric generator (LM-FTG) for vibration energy harvesting. In this device, the fluidity of liquid is used to increase sensitivity to vibration for better low-frequency response and multidirectional vibration energy harvesting capability. The freestanding power generation mode is able to increase power generation stability. Experiments show that the bandwidth of LM-FTG can almost cover the entire sweep frequency range, and a 10 μF capacitor can be charged to 6.46 V at 7.5 Hz in 60 s by LM-FTG. In particular, 100 LEDs are illuminated in the low-frequency environmental experiment successfully. The proposed LM-FTG can work in low frequency with large working bandwidth, which provides an effective method for energy harvesting of low-frequency and multidirectional vibrations.

Keywords: vibration energy harvesting, liquid-metal-based, freestanding, low-frequency, multidirectional, broadband

OPEN ACCESS

Edited by:
Miao Yu,
Chongqing University, China

Reviewed by:
Yancheng Li,
University of Technology Sydney, Australia
Junlei Wang,
Zhengzhou University, China

****Correspondence:***
Huaxia Deng
hxdeng@hfut.edu.cn

Specialty section:
This article was submitted to Smart Materials, a section of the journal Frontiers in Materials

Received: *08 April 2021*
Accepted: *07 June 2021*
Published: *06 July 2021*

Citation:
Deng H, Zhao Z, Jiao C, Ye J, Zhao S, Ma M and Zhong X (2021) A Liquid-Metal-Based Freestanding Triboelectric Generator for Low-Frequency and Multidirectional Vibration. Front. Mater. 8:692273. doi: 10.3389/fmats.2021.692273

1 INTRODUCTION

Internet of Things technology and distributed sensor networks have gradually become the development trend of society, such as wearable devices, smart home appliances, and marine monitoring buoys. They are distributed in all aspects of our lives. These devices can only be powered by distributed independent power sources, and the batteries need to be replaced one by one to ensure the reliability of the device, which will greatly increase maintenance costs (Kim et al., 2017; Yildirim et al., 2017). To convert energy from nature, such as light energy (Park et al., 2016; Kim et al., 2015; Wen et al., 2016), heat energy (Siddique et al., 2017; Sebald et al., 2009; Kim et al., 2014), vibration energy (Sang et al., 2019; Li et al., 2019; Wang et al., 2018b), and so on (Starner, 1996; Guo et al., 2016), has become an effective solution (Yu et al., 2019; Jiang et al., 2018; Pu et al., 2018). A wearable textile battery (Lee et al., 2013), charged by polymer solar cells, can effectively harvest the light energy, providing enough power to light up nine LEDs. But, this kind of energy harvester generally has a poor energy harvesting effect because of the small area of the surface and its susceptibility to the environment, such as the night and cloudy days. Although some designs that harvest heat energy to power the devices have been proposed, they are very sensitive to the temperature and humidity of the environment (Kyono et al., 2003). Vibration energy is an inherent solution to harvest the energy from nature and is not so sensitive to environmental factors such as

light intensity, temperature, and humidity (Rome et al., 2005; Dai et al., 2012). Vibration occurs widely in nature, for example, in the form of human walking, ocean waves, and vibration of mechanical systems. Typically, these vibrations are low frequency, multidirectional, and broadband, which means that traditional electromagnetic energy harvesters (EMGs) are not suitable (Yang et al., 2010; Zuo et al., 2010; Miki et al., 2012).

The reason why EMG is not suitable is that EMG is based on Faraday's law of electromagnetic induction, which means that it relates to the time derivative of the electric field (Khaligh et al., 2010; Siddique et al., 2015). So, EMG is generally suitable for high-frequency situations (above 50 Hz) (Zi et al., 2016; Zhu et al., 2019). Although many people have been working to improve the EMG's capability to operate at low frequencies over the years, it has not been effective for vibrations below 5 Hz because of its incompatibility (Fan et al., 2018; Yildirim et al., 2017a). In addition to EMG, there are some designs that harvest vibration energy with piezoelectric energy harvesters (PEHs) (Zeng et al., 2013; Wei et al., 2013; Safaei et al., 2019; Xiujian et al., 2018). However, PEHs have a common problem: considering the low rate of open-circuit voltage, and piezoelectric modules are often used in series in order to reach the right voltage, which increases the volume of the device. Due to the limited range of the bearing capacity, piezoelectric materials require frequent replacement during usage (Saadon and Sidek, 2011; Liu et al., 2011; Jung et al., 2017).

A triboelectric nanogenerator (TENG) uses the coupling of the triboelectric effect and the electrostatic induction effect, which determine the excellent performance of the TENG in the low-frequency range (Zhang et al., 2014; Qian et al., 2020; Hou et al., 2018; Wang S. et al., 2020; Gao et al., 2018; Wang Z. et al., 2020; Liu et al., 2020a, b). An optimized TENG-based insole designed by Wang (Hou et al., 2013) can harvest the energy of unidirectional vibration excited by contact separation between feet and insoles, which can provide enough power to light up 30 LEDs simultaneously. A self-powered backpack (Yang et al., 2013), which is $5cm \times 7.5cm \times 20cm$ and weighs 2 kg, has been designed to harvest vibration energy and can light up 40 LEDs. It has been proposed to add the bistable system (Deng et al., 2019a; Deng et al., 2019b; Harne and Wang, 2013), which increases the complexity of the structure and the weight of the system, on the TENG-based harvester to broaden the frequency band (Yildirim et al., 2017b). Although these designs can be used to harvest vibration energy, it is difficult to satisfy the requirements of low-frequency, multidirectional, and broadband vibration at the same time. The proposal of using liquid as the friction material provides a new method to solve the problem (Zheng et al., 2014; Chen et al., 2016). Due to the fluidity of liquid, the liquid has a better response to vibration, especially for low-frequency, multidirectional, and broadband vibration (Zhang et al., 2016; Xie et al., 2020). Water as a kind of liquid has previously been proven to be the friction material, but this type of TENG generally does not have good energy conversion capability (due to the limitations of free electrons in water) (Lin et al., 2013). A liquid-metal-based contact-sliding triboelectric principle (Tang et al., 2015) has been proposed, which proves that the liquid metal can also be used as the friction material. The output charge density of this way is 4–5 times that of the TENG, which is a solid film electrode under the same conditions. Typically, there have been some designs of triboelectric generators based on the liquid metal, but they use the liquid metal as a conductor rather than this principle (Wang et al., 2018a; Yang et al., 2018). Therefore, in order to harvest vibration energy, a triboelectric device based on the liquid metal can be designed.

Here, we present a liquid-metal-based freestanding triboelectric generator (LM-FTG) to solve the problem of vibration energy harvesting. The power generation mode of LM-FTG is freestanding in order to ensure the stability of power generation, which avoids the situation that the liquid metal cannot contact the metal electrode to generate electricity. We show the details of the specific electricity generation process. The multidirectional harvesting capability and low-frequency adaptability are proved by intuitive experiments and theoretical analysis. In the experiments, we perform an inertial frequency-sweep experiment, which proves the multidirectional and broadband vibration harvesting capability of the device. The power experiment under inertial force constant frequency excitation further proves superiority of different working modes and the low-frequency response of LM-FTG. Through the low-frequency environmental experiment, the practicality of this device is proved.

2 DESIGN AND MECHANISM

As shown in **Figure 1A**, LM-FTG, which consists of an aluminum alloy threaded cylinder, two aluminum alloy threaded caps, a 3D printed material sleeve (polylactic acid), a suitable amount (the height of the liquid level is about a quarter of the height of the container) of the liquid metal (mercury, gallium, or gallium–indium), two triboelectric components, and two silicone seals, is similar in shape to a cylindrical container. In order to prevent the liquid metal from conducting with the external metal shell, which enhances the overall impact resistance, a 3D printed material sleeve is used to isolate the liquid metal from the metal shell. The silicone sealing ring is placed between the aluminum alloy threaded cap and the triboelectric component. By screwing the threaded cap tightly, the container is sealed. When LM-FTG is subjected to external excitation, the internal liquid metal collides between the surfaces of Kapton at both sides to generate electricity. The detailed information of LM-FTG is shown in **Supplementary Figure S1**.

It is worth noting that, in the selection of the liquid metal, we put the droplets of mercury, gallium, and water on the Kapton's surface, respectively, and observed their surface morphology. As shown in **Figure 2**, the droplets of mercury and gallium on the Kapton's surface basically maintain a spherical droplet state while the water is flat on the surface. This proves not only that gallium can be easily separated from Kapton without adhesion but also that mercury has this property. However, compared to mercury, gallium is easier to oxidize in the air and forms an oxide layer that is difficult to detach on the Kapton's surface. In response to this phenomenon, we chose mercury, which is extremely difficult to oxidize, as the liquid metal in LM-FTG.

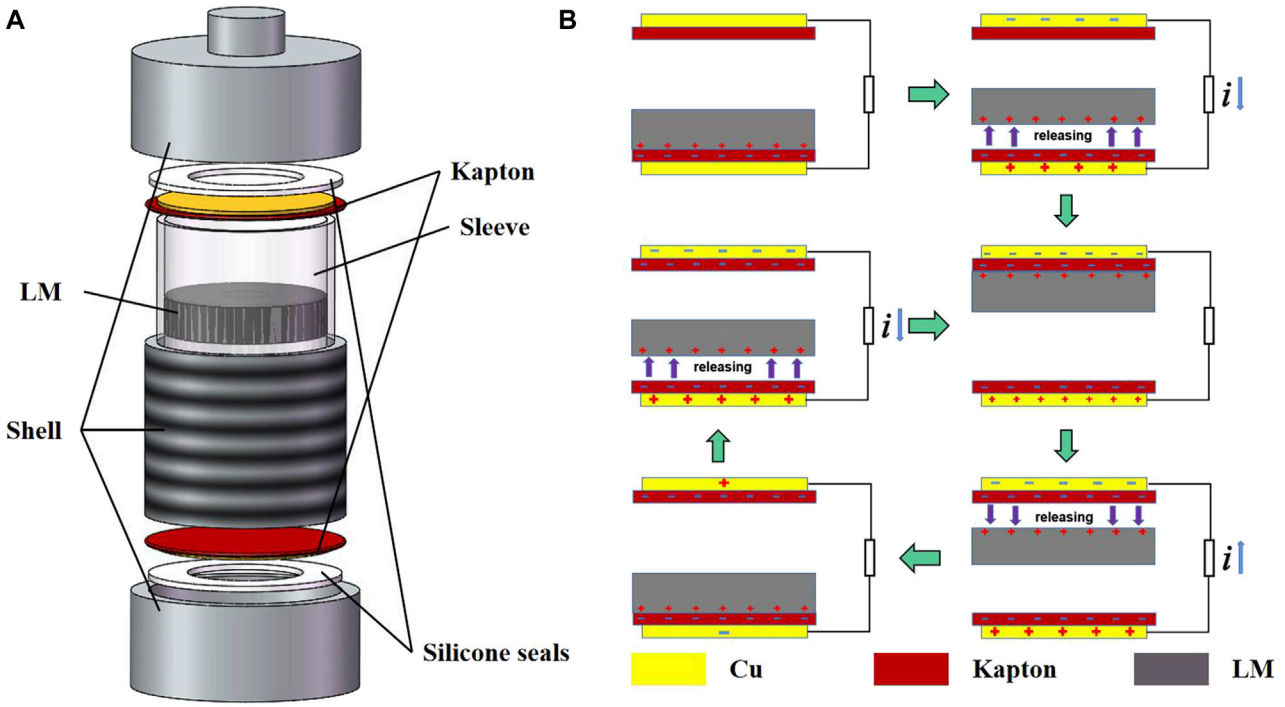

FIGURE 1 | Working principle of LM-FTG. **(A)** Schematic illustration showing the device configuration of LM-FTG; **(B)** step-by-step illustration showing the working principle of LM-FTG.

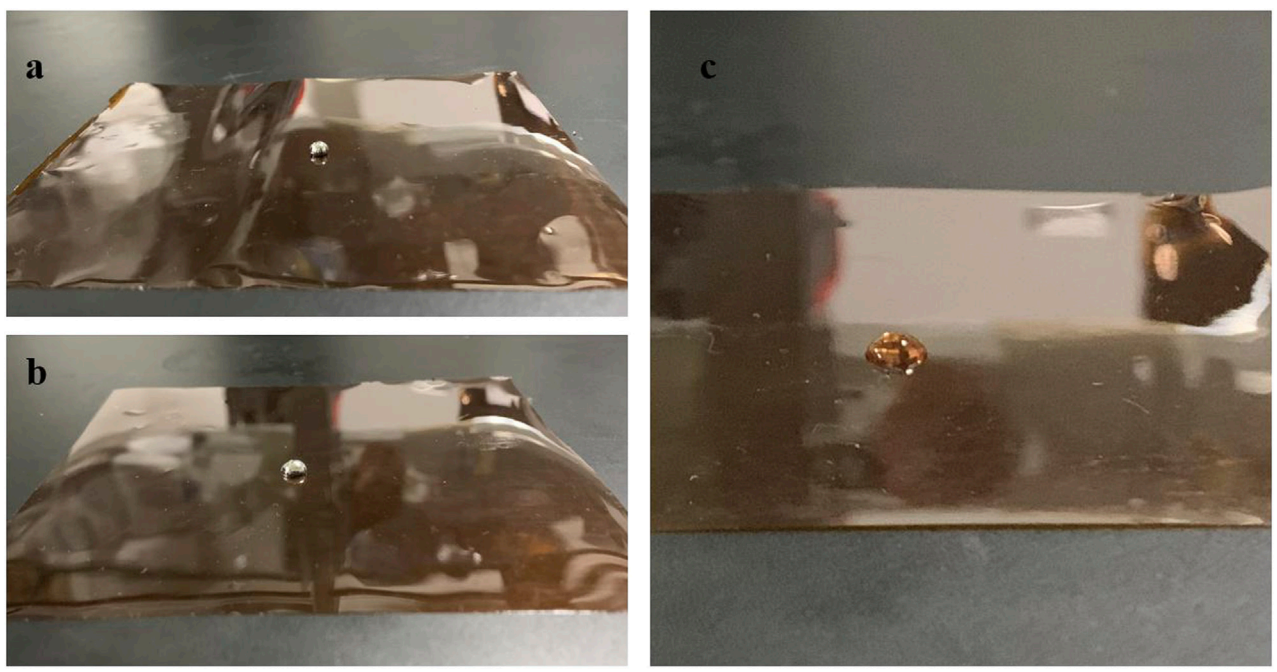

FIGURE 2 | Droplets of mercury, gallium, and water on Kapton's surface. **(A)** Mercury; **(B)** gallium; and **(C)** water.

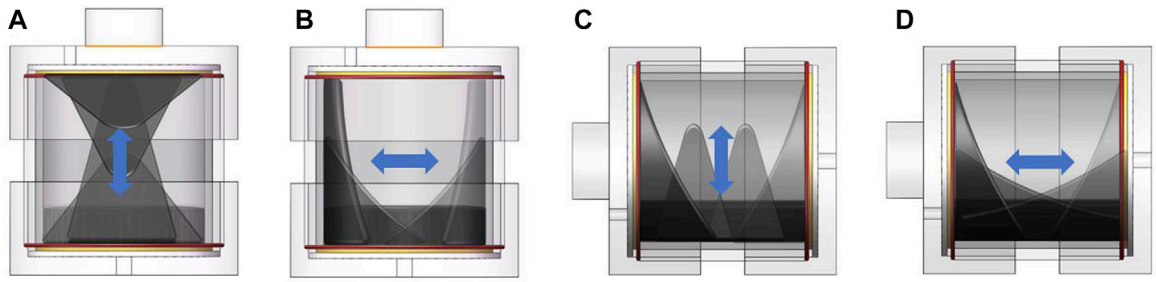

FIGURE 3 | Internal liquid flow. **(A)** Liquid flow in the VV mode; **(B)** liquid flow in the VH mode; **(C)** liquid flow in the HV mode; and **(D)** liquid flow in the HH mode.

A complete cycle of the electricity generation process is shown in **Figure 1B**. The contact-separation movement between the liquid metal and the triboelectric components is driven by the excitation of the outer casing. First, after pouring the liquid metal into the container, the liquid metal makes contact with the Kapton surface on one side. Due to the different capabilities of the liquid metal and Kapton to absorb electrons, electrons are transferred from the liquid metal onto the Kapton's surface, causing positive charges at the interface of the liquid metal and negative charges on the Kapton's surface. Then, the two materials are separated by the external excitation, and a potential difference is formed between them. In order to counteract the electric field, electrons will flow from the lower surface copper electrode to the upper surface copper electrode, which forms a reverse current. As the liquid metal continues to rise, it will collide with the upper Kapton's surface. Similar to the previous process, the liquid metal also undergoes charge transfer with the upper Kapton. Finally, during the liquid-metal drop process, due to the potential difference between the liquid metal and the upper surface, it will produce a current in the opposite direction to the previous process. Therefore, the pulse output of the entire process exhibits the characteristics of AC. In particular, this freestanding power generation mode causes the device to contact-separate the upper and lower surfaces twice in one power generation cycle, so it is equivalent to two power generations, which increases the number of power generations and improves power generation efficiency. In addition, compared with the first proposed sliding friction power generation mode, this power generation mode does not need to ensure that the internal liquid metal is always in contact with the conductor, which increases the stability of power generation.

Since the internal liquid metal can generate electricity just by impacting and shaking between Kapton at both sides, we set four working modes, which are vertical placement and vertical vibration (VV mode), vertical placement and horizontal vibration (VH mode), horizontal placement and vertical vibration (HV mode), and horizontal placement and horizontal vibration (HH mode), according to the LM-FTG's placement and vibration direction. **Figure 3** shows the liquid flow mode under different working modes. In order to prove that the vibration modes are similar to the pictures, we put the liquid metal in the transparent tube and shook the hand to simulate vibration (see **Supplementary Movies S1–S4**). It can be seen from the video that the liquid metal can impact surfaces of both sides regardless of the working mode under external excitation. So, the multidirectional vibration harvesting capability of LM-FTG can also be demonstrated.

In order to prove that the liquid metal can better respond to external low-frequency vibration, we develop the fluid field equations for one of the working modes and estimate the relationship between the liquid free surface wave height and the frequency of external excitation. As shown in **Figure 4A**, we assume that LM-FTG works in the VH mode and set up an inertial frame and a moving coordinate system. The height of the liquid surface is represented by h, and the radius of the circular surface of the cylindrical container is represented by R.

Assuming the container is laterally excited in the x-axis direction,

$$X(t) = A\sin\omega t, \tag{1}$$

where A and ω are the excitation amplitude and frequency, respectively. Since the analysis can be simplified if the fluid equations are linearized for small displacements, the linearized fluid field equations take the form

$$\nabla^2\tilde{\Phi} = 0, \tag{2}$$

$$\left.\frac{\partial\tilde{\Phi}}{\partial r}\right|_{r=R} = 0, \left.\frac{\partial\tilde{\Phi}}{\partial z}\right|_{z=-h} = 0, \tag{3}$$

$$g\eta - \frac{\partial\tilde{\Phi}}{\partial t} + \ddot{X}r\cos\theta = 0,\ at\ z = \eta(r,\theta,t), \tag{4}$$

$$-\frac{\partial\tilde{\Phi}}{\partial z} = \frac{\partial\eta}{\partial t}\ \text{at}\ z = \eta(r,\theta,t). \tag{5}$$

The dynamic and kinematic free surface conditions in **Eq. 4** and **Eq. 5** can be combined into

$$g\frac{\partial\tilde{\Phi}}{\partial z} + \frac{\partial^2\tilde{\Phi}}{\partial t^2} = \dddot{X}r\cos\theta. \tag{6}$$

A typical solution of **Eq. 2** subject to conditions in **Eq. 3** is

$$\tilde{\Phi} = \sum_{n=1}^{\infty}[A_n(t)\cos\theta + B_n(t)\sin\theta]J(\xi_n r/R)\frac{\cosh[\xi_n(z+h)/R]}{\cosh\xi_n h/R}, \tag{7}$$

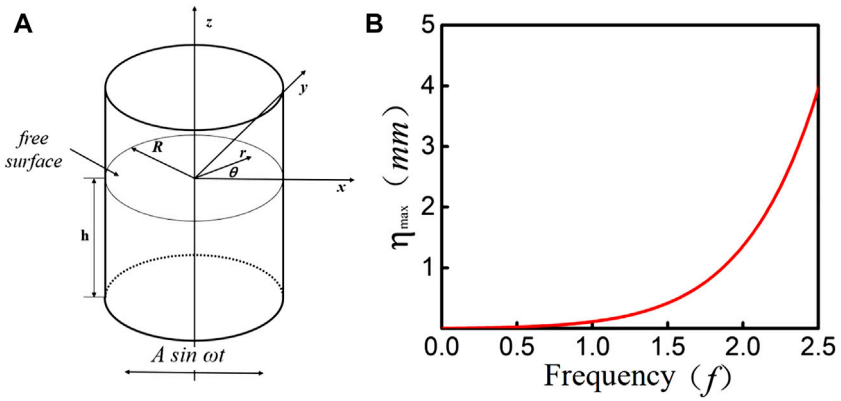

FIGURE 4 | (A) Cylindrical tank under sinusoidal lateral excitation. **(B)** Relationship between maximum wave height η_{max} and external excitation frequency ω.

where $\xi_n = (2n-1)\pi/2$. J (.) is the Bessel function of the first kind. A_n and B_n are time dependent to be determined from the free-surface initial conditions. Under the constraints of the free-surface condition in **Eq. 6**, we can get

$$A_n(t) = -\frac{A\omega^3 F_n}{(\omega_n^2 - \omega^2)\cosh(\xi_n h/R)}\cos\omega t, B_n(t) = 0, \quad (8)$$

where ω_n is the multiorder natural frequency of the liquid and $\omega_n^2 = (g\xi_n\pi)/R\tanh(\xi_n h/R)$.

Substituting **Eq. 8** into **Eq. 7**, **Eq. 7** can be rewritten as

$$\tilde{\Phi} = -A\omega\cos\theta\cos\omega t \times \sum_{n=1}^{\infty}\left[\frac{2R}{(\xi_n^2-1)}\frac{\omega^2}{(\omega_n^2-\omega^2)}\frac{J(\xi_n r/R)}{J(\xi_n)}\frac{\cosh[\xi_n(z+h)/R]}{\cosh(\xi_n h/R)}\right]. \quad (9)$$

The total potential function is the sum of the fluid perturbed function $\tilde{\Phi}$ and the tank potential function $\Phi = -A\omega\cos\theta\cos\omega t$, that is,

$$\Phi = -A\omega\cos\theta\cos\omega t \times\left\{r + \sum_{n=1}^{\infty}\left[\frac{2R}{(\xi_n^2-1)}\frac{\omega^2}{(\omega_n^2-\omega^2)}\frac{J(\xi_n r/R)}{J(\xi_n)}\frac{\cosh[\xi_n(z+h)/R]}{\cosh(\xi_n h/R)}\right]\right\}. \quad (10)$$

Substituting **Eq. 10** into condition **Eq. 4** gives the surface wave height

$$\eta = \frac{A\omega^2}{g}\cos\theta\cos\omega t\left[r + \sum_{n=1}^{\infty}\frac{2R}{(\xi_n^2-1)}\frac{\omega^3}{(\omega_n^2-\omega^2)}\frac{J(\xi_n r/R)}{J(\xi_n)}\right]. \quad (11)$$

The maximum wave height occurs at $r = R$, $\theta = 0$, and $\omega t = \pi/2$ and is given by the following expression:

$$\eta_{max} = \frac{A\omega^2}{g}\left[R + \sum_{n=1}^{\infty}\frac{2R}{(\xi_n^2-1)}\frac{\omega^3}{(\omega_n^2-\omega^2)}\right]. \quad (12)$$

We set the amplitude A = 0.001 m and substitute the relevant parameters of LM-FTG into the expression (R = 0.015 m and h = 0.015 m) to obtain the maximum wave height of the liquid surface η_{max} as a function of the external excitation frequency ω. As shown in **Figure 4B**, although the external amplitude is only 0.001 m, the maximum wave height can reach 1.3 mm under the external vibration frequency of 2 Hz. Typically, η_{max} shows a nonlinear growth with the increase of the ω. This proves that the liquid in the tank has a remarkable response to the low-frequency vibration in the VH mode. In addition, although we only conduct a specific analysis for the VH mode, since the liquid metal is in the same tank, no matter which working mode is used, the form of ω_n and the free-surface condition of the liquid metal are not changed. It also means the liquid metal can have great response in each working mode, which reflects the device's capability to harvest multidirectional vibrations.

3 EXPERIMENT

In order to explore the performance and characteristics of LM-FTG, we conducted two major experiments based on the experimental environment. The first part is an experiment conducted on a vibrating table, mainly to explore the material properties and multidirectional vibration harvesting capability of LM-FTG. The experimental results also play a guiding role in the subsequent experiments. This part of the experimental system mainly consists of a vibration table (Sushi DC-1000–15) and its controller (RC-3000), a digital multimeter (ZLG DMM6001), a computer, and a resistance box (see **Supplementary Figure S2**).

The second part of the experiment is a low-frequency environmental experiment, which proves the practicality of this device.

3.1 Vibrating Table Experiment

For the experiment on the vibration table, it is mainly divided into three parts, namely, basic output experiment, frequency-sweep experiment, and power experiment. Firstly, the basic output experiment is used to measure the internal resistance of the material, and then, a frequency-sweep test is used to not only investigate the influence of the working modes on the test data

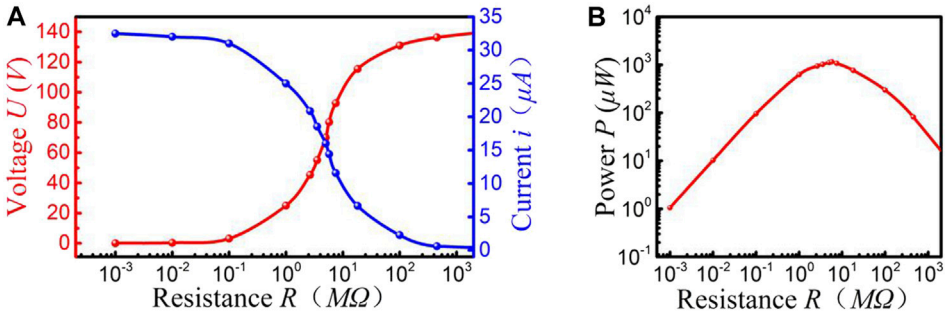

FIGURE 5 | Basic output of the material. **(A)** Output voltage and output current of Kapton under different resistance values. **(B)** The power of Kapton at different resistance values.

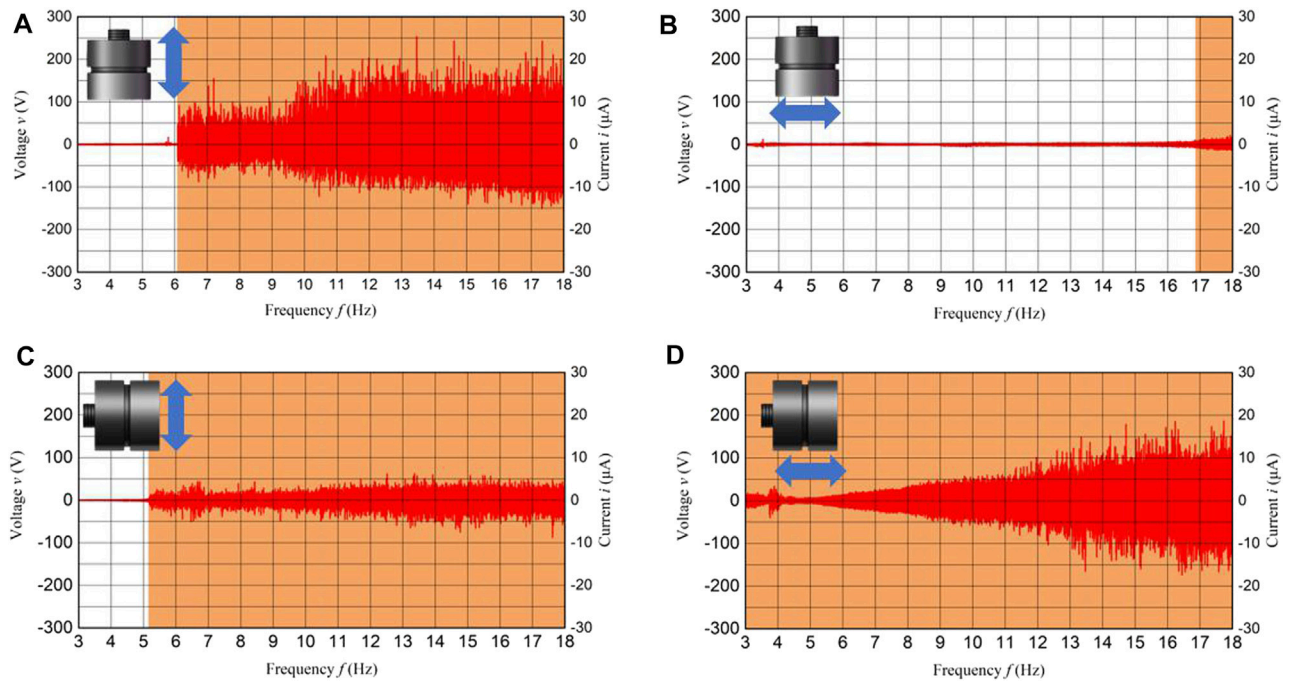

FIGURE 6 | Results of the inertial-force frequency-sweep test under 13 mm peak-to-peak excitation at 3–18 Hz sweep frequency: **(A)** Output voltage and current of LM-FTG in the VV mode. **(B)** Output voltage and current of LM-FTG in the VH mode. **(C)** Output voltage and current of LM-FTG in the HV mode. **(D)** Output voltage and current of LM-FTG in the HH mode.

but also verify broadband output. The final power experiment explores the continuous discharge capability of LM-FTG at low frequencies and further verifies the effects of different working modes, which plays a guiding role in the low-frequency environmental experiment.

3.1.1 Basic Output

In order to measure the maximum output power and power density of LM-FTG in the frequency-sweep experiment, the basic output of LM-FTG needs to be determined to infer the internal resistance. The output voltage, output current (**Figure 5A**), and power of LM-FTG (**Figure 5B**) is measured at constant frequency (10 Hz) and peak-to-peak value (15 mm) excitation. We sequentially change the resistance of the resistance box to measure the output voltage and current of LM-FTG. Then, the optimum resistance of the generator is determined by obtaining the maximum output power. Through the experimental results and drawing, it can be found that the maximum output power is obtained when the resistance is 8 MΩ.

3.1.2 Frequency Sweep

According to the analysis of the theoretical part, the working modes of LM-FTG have an impact on its power generation capability. Two fixed LM-FTG's bases are fixed on the vibration table, and the vertical and horizontal vibration tables are used to test LM-FTG. In order to explore the power generation capability and working bandwidth of each mode, we perform an inertial-force frequency-

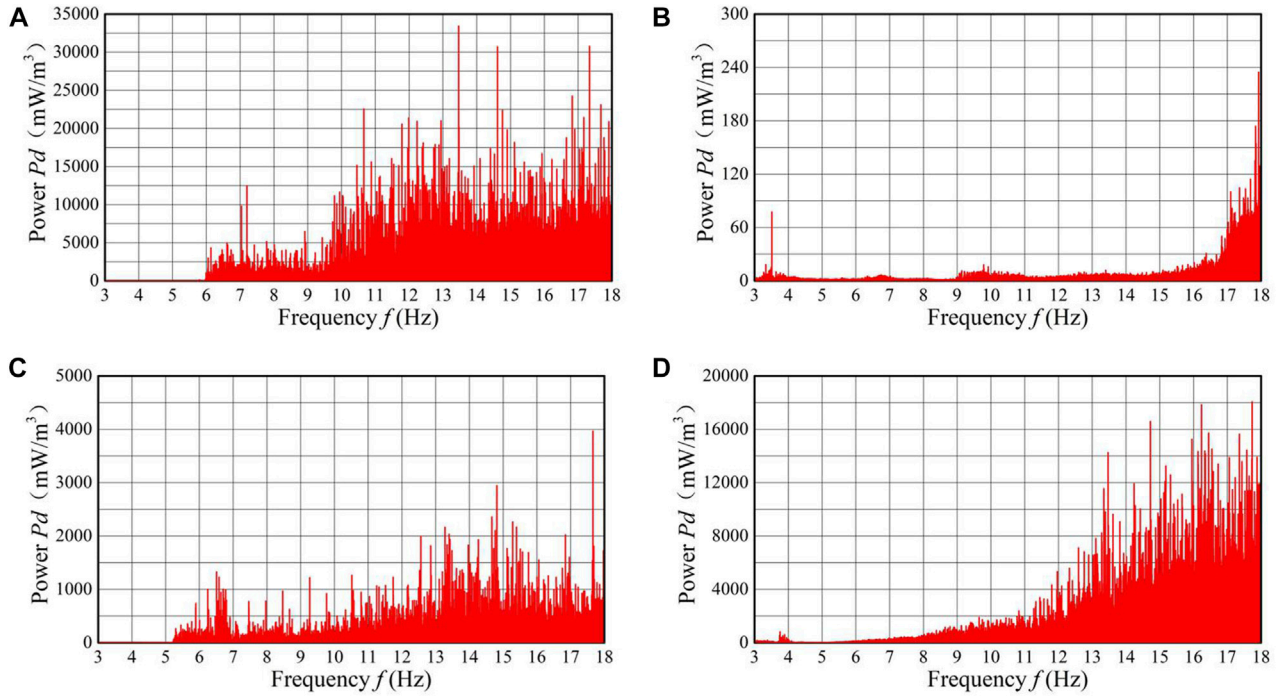

FIGURE 7 | Power density of the frequency-sweep test under 13 mm peak-to-peak excitation at 3–18 Hz sweep frequency. **(A)** Power density of LM-FTG in the VV mode. **(B)** Power density of LM-FTG in the VH mode. **(C)** Power density of LM-FTG in the HV mode. **(D)** Power density of LM-FTG in the HH mode.

sweep experiment in four working modes (see **Supplementary Figure S3**). **Figure 6** shows the frequency-domain performance results of LM-FTG under an excitation in which the peak-to-peak value is 13 mm and the frequency f sweep is from 3 to 18 Hz at a frequency rise rate of 0.05 Hz/s.

It can be seen from **Figure 6A** that when LM-FTG is in the VV mode, the output of LM-FTG always shows an upward trend after 6.2 Hz (the effective frequency bands, which are the colored areas, are defined as the frequency bands, where the output voltage exceeds 10 V), and the peak output voltage and current can reach 252 V and 25.2 μA, respectively. However, in the case of the VH mode (**Figure 6B**), LM-FTG has a small output after 16.2 Hz, and the peak output can only reach 15 V and 0.2 μA, which is not ideal. **Figures 6C**,D show the situation of horizontal placement. It can be seen from **Figure 6C** that, for the vertical vibration, LM-FTG starts to show an obvious output after 5.2 Hz. Although the peak output can only reach 58 V and 5.8 μA, the output is relatively stable, which covers the entire frequency band after 5.2 Hz. In particular, in the case of horizontal vibration, the output, which is shown in **Figure 6D**, achieves a full-band coverage of 3–18 Hz, and the peak output can reach 181 V and 1.8 μA. Based on the abovementioned data, it can be seen that, in the case of vertical placement, although the maximum peak output in the four modes can be achieved in vertical vibration and the frequency band width is great, the response to the horizontal vibration is poor, which hardly has output and is difficult to meet the energy harvesting of multidirectional vibrations. When placed horizontally, although the peak output does not shine in the two vibration directions, it has a wide frequency band and even achieves full-band coverage under horizontal vibration, which is more in line with the requirements of vibration energy harvesting. It is worth noting that LM-FTG has a good effect in both VV and HH modes. The reason is that the vibration direction in these two modes is kept parallel to the tank body, which can ensure that the liquid metal is better contacted and separated from the Kapton on both sides.

The power density of LM-FTG can be calculated according to the formula $Pd = U^2/(RV)$ (U, R, and V are the output voltage, the load resistance, and the effective volume, respectively). According to the internal resistance of the device in the first part of the experiment, we chose a 8 MΩ load resistor to get the best power density. The optimal power density in the four modes is shown in **Figure 7**. It is worth noting that the power density in the case of vertical placement and vertical vibration can reach 33000 mW/ m^3. The use of the liquid metal to generate electricity can get the ultra-high power density, so that this device can output high energy in a small volume and is suitable for different environments.

In order to explore the impact of different amplitudes on LM-FTG, we performed sweep experiments on LM-FTG with the peak-to-peak values of 9 and 16 mm (see **Supplementary Figure S6**). Although the output voltage and current are proportional to the amplitude in some working modes, there is not much difference in the working frequency band and output of LM-FTG under these three amplitude conditions.

3.1.3 Power Experiment

In order to verify LM-FTGs ability of vibration harvesting at low frequency and further prove the conclusion about the influence of

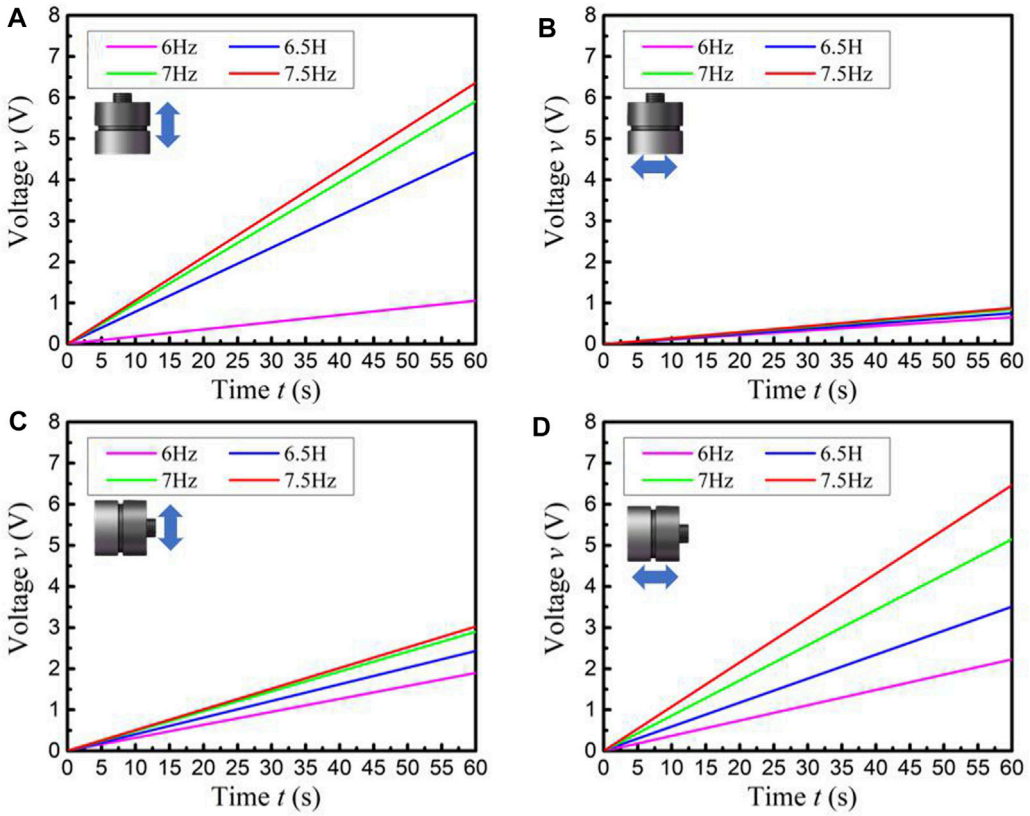

FIGURE 8 | Voltage of the 10 μF capacitor charged by LM-FTG. **(A)** Low-frequency response of LM-FTG in the VV mode. **(B)** Low-frequency response of LM-FTG in the VH mode. **(C)** Low-frequency response of LM-FTG in the HV mode. **(D)** Low-frequency response of LM-FTG in the HH mode.

working modes on harvesting capability, we performed the power experiment using the capacitor to charge in four modes like the frequency-sweep experiment. The vibration amplitude of the vibration table is set to 13 mm and the excitation frequencies applied are 6, 6.5, 7, and 7.5 Hz. The output of LM-FTG is connected to a 10 μF electrolytic capacitor to charge it, and the capacitor voltage is measured by a digital multimeter.

It can be seen from **Figure 8B** that, in the vertical placement, the output power of LM-FTG is very low when excited by the horizontal direction. Within 60 s, the voltage of the capacitor is below 0.4 V. **Figure 8A** shows the results when the vibration direction is vertical. The output power of LM-FTG is not ideal at 6 Hz, and the capacitor is only charged to 1.05 V. As the frequency gradually increases to 6.5, 7, and 7.5 Hz, the voltage of the capacitor suddenly increases to 4.68, 5.90, and 6.36 V. In the horizontal placement, the voltage of the capacitor reaches 1.89, 2.43, 2.89, and 3.02 V within 60 s at the excitation frequencies of 6, 6.5, 7, and 7.5 Hz when excited in the vertical direction. When excited by the vertical direction, the output voltage increases to 2.22, 3.50, 5.14, and 6.46 V. At horizontal placement, not only the device shows great harvesting capability for both directions of vibration but also the harvesting of low-frequency vibration energy is better than the vertical placement. In general, similar to the conclusion of the sweep-frequency experiment, LM-FTG has a good effect when the vibration direction is parallel to the tank body.

3.2 Low-Frequency Environmental Experiment

Since the walking vibration not only has the characteristics of low frequency, multidirection, and broadband but also is very common, we use the walking experiment to prove the practicality of LM-FTG. In the frequency-sweep experiment, the influence of the placement on the harvesting capability is verified. Here, in order to verify the impact of the placement in practice, we tied two identical LM-FTGs to the two calves in two ways (**Figure 9**) and conducted the walking experiment. In particular, for verifying the effect of walking speed on the LM-FTG's harvesting capability, we measure the output voltage of LM-FTG and the acceleration of walking (see **Supplementary Figure S4**) at speeds of 0.8, 1.2, 2 ,and 4 m/s.

Figure 9C shows the output voltage of LM-FTG under horizontal placement. It can be seen intuitively that the output voltage of LM-FTG increases with the increase in walking speed, which is an obvious proportional relationship. As shown in **Figure 7C**, the peak output voltage of LM-FTG is only 48 V at a walking speed of 0.8 m/s, while the peak output voltages of 1.2, 2, and 4 m/s reach 71, 82, and 169 V, respectively. The huge impact of walking speed on the open circuit

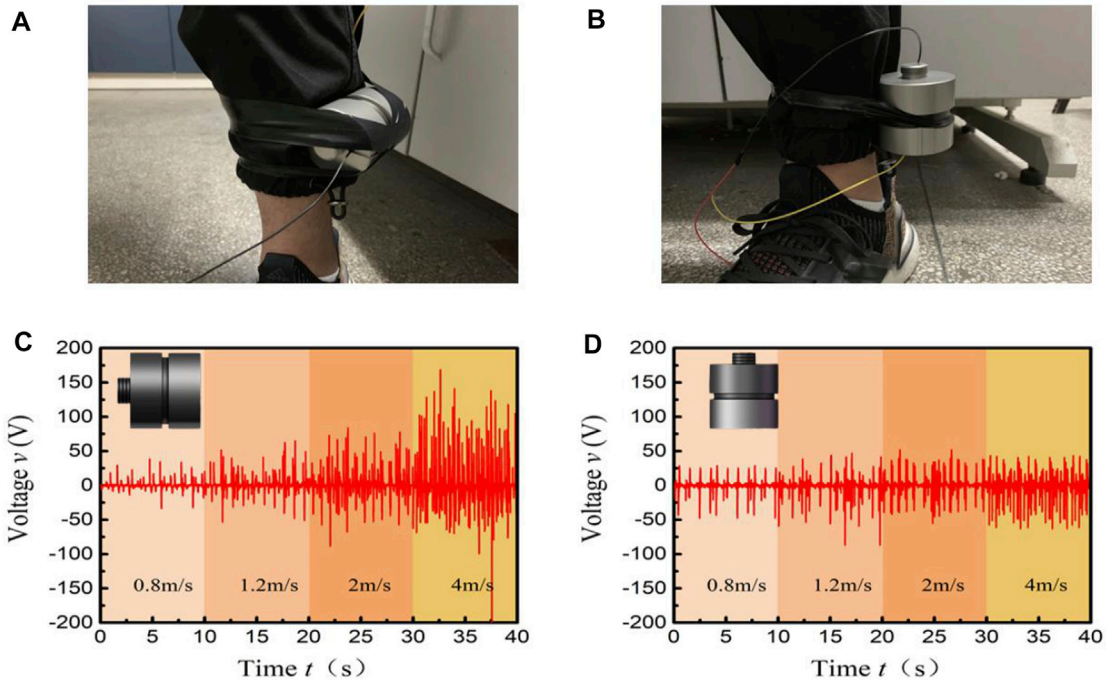

FIGURE 9 | (A) LM-FTG in horizontal placement.**(B)** LM-FTG in vertical placement. **(C)** Output voltage of LM-FTG in horizontal placement. **(D)** Output voltage of LM-FTG in vertical placement.

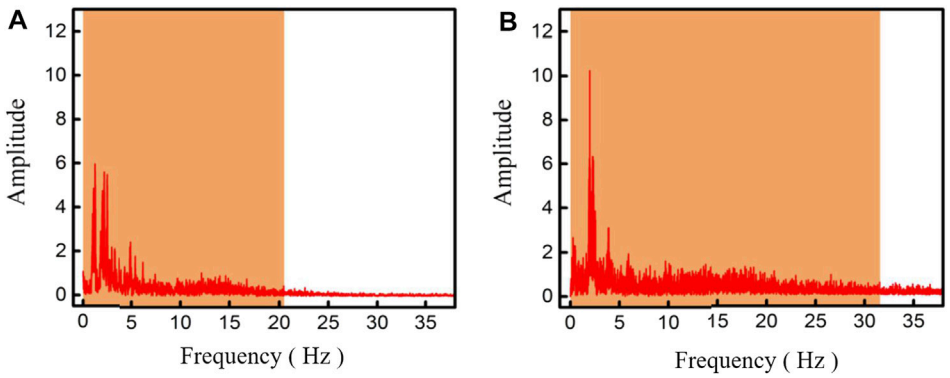

FIGURE 10 | (A) Spectrogram of walking.**(B)** Spectrogram of running.

voltage was verified. However, compared with the output voltage of LM-FTG in the vertical mode shown in **Figure 9D**, it can be seen that the difference of the output voltages is not obvious at the four walking speeds, and the peak output voltages do not exceed 50 V at most. The conclusions drawn in the frequency-sweep experiment are verified in practice.

In order to investigate the vibration frequency of walking, we measure the acceleration (see **Supplementary Figure S3**) of walking at the speed of 0.8 and 4 m/s. **Figure 10A** shows the spectrograms obtained by Fourier transform of the measured acceleration data at walking speeds of 0.8 and 4 m/s. As can be seen from **Figure 10A**, at a walking speed of 0.8 m/s, most of the frequency components are concentrated around 2.4 and 5 Hz. In this case where the effective band is defined as a band having an amplitude of 0.4 or more, the vibration frequency ranges from 0 to 20.82 Hz. This proves that the general walking vibration frequency band is wide and mainly concentrated in the low-frequency range. **Figure 10B** shows the spectrum at a walking speed of 4 m/s. Most of the frequency components are also concentrated below 5 Hz, but the frequency range can range from 0 to 32.03 Hz. By comparison, it can be seen that most of the frequency components are concentrated below

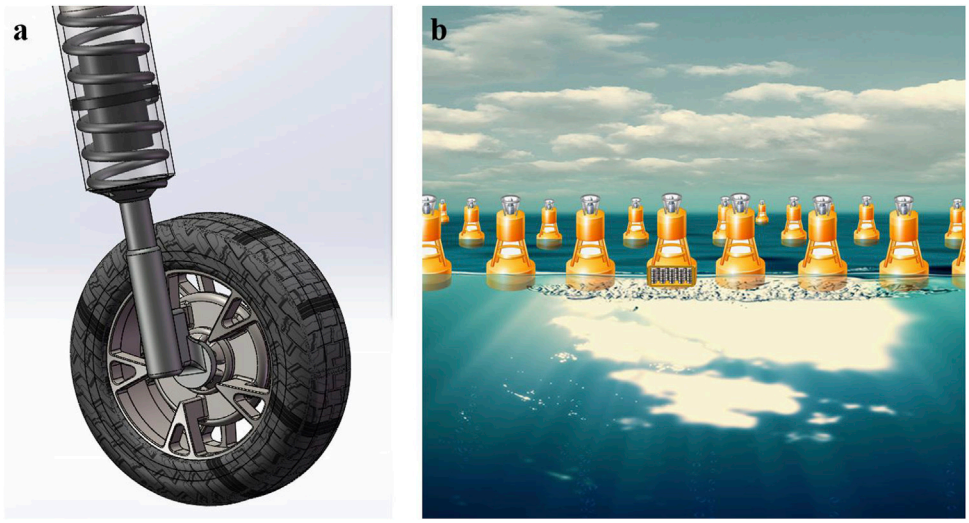

FIGURE 11 | (A) LM-FTG in car suspension.**(B)** LM-FTG in the ocean buoy.

5 Hz, but the increase in speed increases the bandwidth. In summary, it can be shown that the vibration frequency of walking is mostly concentrated in 0–3 Hz, and the power generation experiment under actual walking can prove the LM-FTG's harvesting capability in this frequency band.

In order to more intuitively demonstrate the power generation capability of LM-FTG, we wanted to light up LEDs with LM-FTG in actual walking. According to the previous experiments, we attached LM-FTG to the calf under the horizontal mode and it successfully lit up 100 series-connected LEDs (see **Supplementary Movie S5**).

4 CONCLUSION

In order to harvest vibration energy which is low frequency, multidirectional, and broadband, a triboelectric generator, which bases on the liquid metal and freestanding power generation mode, has been proposed. The device utilizes the fluidity of the liquid to more efficiently harvest low-frequency and multidirectional vibrations. Also, the freestanding power generation mode is used to decrease the structural complexity and ensure the stability of power generation. The frequency-sweep experiment shows that the difference of the working modes has a great influence on the power generation capability. The multidirectional vibration can be harvested and the working frequency band of LM-FTG is wide. In addition, the peak output can reach up to 252 V and 25.2 μA, and a 10 μF capacitor can be charged to 6.46 V at 7.5 Hz in 60 s by LM-FTG. In the low-frequency environmental experiment, the peak output voltage of LM-FTG under the horizontal mode with 4 m/s of the walking speed can reach 169 V and it can light up 100 LEDs in walking.

In addition, although the experiment was only carried out under the condition of wearing, the device can also be used in more fields. As shown in **Figure 11**, LM-FTG can be placed in the marine buoy to harvest wave energy from ocean waves or placed in the car suspension to harvest the vibrational energy of the car. So, we believe that LM-FTG not only provides a welcome boost for the development of a vibration energy harvester but also has a broader application prospect.

DATA AVAILABILITY STATEMENT

The raw data supporting the conclusions of this article will be made available by the authors, without undue reservation.

AUTHOR CONTRIBUTIONS

HD, ZZ, and CJ conceived and designed the manuscript. JY, SZ, MM, and XZ revised it. All authors contributed to the article and approved the submitted version.

FUNDING

The authors appreciate the support of the National Natural Science Foundation of China (Grant Nos. 11872167, 51675156, 51775164, and 51705122) and Natural Science Foundation of Anhui 281 Province (No. 1908085J15).

SUPPLEMENTARY MATERIAL

The Supplementary Material for this article can be found online at: https://www.frontiersin.org/articles/10.3389/fmats.2021.692273/full#supplementary-material

REFERENCES

Chen, J., Guo, H., Zheng, J., Huang, Y., Liu, G., Hu, C., et al. (2016). Self-Powered Triboelectric Micro Liquid/Gas Flow Sensor for Microfluidics. *ACS Nano* 10, 8104–8112. doi:10.1021/acsnano.6b04440

Dai, D., Liu, J., and Zhou, Y. (2012). Harvesting Biomechanical Energy in the Walking by Shoe Based on Liquid Metal Magnetohydrodynamics. *Front. Energ.* 6, 112–121. doi:10.1007/s11708-012-0186-x

Deng, H., Du, Y., Wang, Z., Ye, J., Zhang, J., Ma, M., et al. (2019a). Poly-stable Energy Harvesting Based on Synergetic Multistable Vibration. *Commun. Phys.* 2, 10. doi:10.1038/s42005-019-0117-9

Deng, H., Ye, J., Du, Y., Zhang, J., Ma, M., and Zhong, X. (2019b). Bistable Broadband Hybrid Generator for Ultralow-Frequency Rectilinear Motion. *Nano Energy* 65, 103973. doi:10.1016/j.nanoen.2019.103973

Fan, K., Liu, S., Liu, H., Zhu, Y., Wang, W., and Zhang, D. (2018). Scavenging Energy from Ultra-low Frequency Mechanical Excitations through a Bi-directional Hybrid Energy Harvester. *Appl. Energ.* 216, 8–20. doi:10.1016/j.apenergy.2018.02.086

Gao, H., Minh, P. T., Wang, H., Minko, S., Locklin, J., Nguyen, T., et al. (2018). High-performance Flexible Yarn for Wearable Piezoelectric Nanogenerators. *Smart Mater. Struct.* 27, 095018. doi:10.1088/1361-665X/aad718

Guo, H., Yeh, M.-H., Lai, Y.-C., Zi, Y., Wu, C., Wen, Z., et al. (2016). All-in-one Shape-Adaptive Self-Charging Power Package for Wearable Electronics. *ACS Nano* 10, 10580–10588. doi:10.1021/acsnano.6b06621

Harne, R. L., and Wang, K. W. (2013). A Review of the Recent Research on Vibration Energy Harvesting via Bistable Systems. *Smart Mater. Struct.* 22, 023001. doi:10.1088/0964-1726/22/2/023001

Hou, T.-C., Yang, Y., Zhang, H., Chen, J., Chen, L.-J., and Lin Wang, Z. (2013). Triboelectric Nanogenerator Built inside Shoe Insole for Harvesting Walking Energy. *Nano Energy* 2, 856–862. doi:10.1016/j.nanoen.2013.03.001

Hou, X., Zhu, J., Qian, J., Niu, X., He, J., Mu, J., et al. (2018). Stretchable Triboelectric Textile Composed of Wavy Conductive-Cloth PET and Patterned Stretchable Electrode for Harvesting Multivariant Human Motion Energy. *ACS Appl. Mater. Inter.* 10, 43661–43668. doi:10.1021/acsami.8b16267

Jiang, Q., Wu, C., Wang, Z., Wang, A. C., He, J.-H., Wang, Z. L., et al. (2018). MXene Electrochemical Microsupercapacitor Integrated with Triboelectric Nanogenerator as a Wearable Self-Charging Power Unit. *Nano Energy* 45, 266–272. doi:10.1016/j.nanoen.2018.01.004

Jung, I., Shin, Y.-H., Kim, S., Choi, J.-y., and Kang, C.-Y. (2017). Flexible Piezoelectric Polymer-Based Energy Harvesting System for Roadway Applications. *Appl. Energ.* 197, 222–229. doi:10.1016/j.apenergy.2017.04.020

Khaligh, A., Peng Zeng, P., and Cong Zheng, C. (2010). Kinetic Energy Harvesting Using Piezoelectric and Electromagnetic Technologies-State of the Art. *IEEE Trans. Ind. Electron.* 57, 850–860. doi:10.1109/TIE.2009.2024652

Kim, B. J., Kim, D. H., Lee, Y.-Y., Shin, H.-W., Han, G. S., Hong, J. S., et al. (2015). Highly Efficient and Bending Durable Perovskite Solar Cells: toward a Wearable Power Source. *Energy Environ. Sci.* 8, 916–921. doi:10.1039/c4ee02441a

Kim, J., Kumar, R., Bandodkar, A. J., and Wang, J. (2017). Advanced Materials for Printed Wearable Electrochemical Devices: a Review. *Adv. Electron. Mater.* 3, 1600260. doi:10.1002/aelm.201600260

Kim, S. J., We, J. H., and Cho, B. J. (2014). A Wearable Thermoelectric Generator Fabricated on a Glass Fabric. *Energ. Environ. Sci.* 7, 1959–1965. doi:10.1039/c4ee00242c

Kyono, T., Suzuki, R. O., and Ono, K. (2003). Conversion of Unused Heat Energy to Electricity by Means of Thermoelectric Generation in Condenser. *IEEE Trans. Energ. Convers.* 18, 330–334. doi:10.1109/TEC.2003.811721

Lee, Y.-H., Kim, J.-S., Noh, J., Lee, I., Kim, H. J., Choi, S., et al. (2013). Wearable Textile Battery Rechargeable by Solar Energy. *Nano Lett.* 13, 5753–5761. doi:10.1021/nl403860k

Li, Y., Shen, W., and Zhu, H. (2019). Vibration Mitigation of Stay Cables Using Electromagnetic Inertial Mass Dampers: Full-Scale experiment and Analysis. *Eng. Structures* 200, 109693. doi:10.1016/j.engstruct.2019.109693

Lin, Z.-H., Cheng, G., Lin, L., Lee, S., and Wang, Z. L. (2013). Water-solid Surface Contact Electrification and its Use for Harvesting Liquid-Wave Energy. *Angew. Chem.* 125, 12777–12781. doi:10.1002/ange.201307249

Liu, H., Tay, C. J., Quan, C., Kobayashi, T., and Lee, C. (2011). Piezoelectric MEMS Energy Harvester for Low-Frequency Vibrations with Wideband Operation Range and Steadily Increased Output Power. *J. Microelectromech. Syst.* 20, 1131–1142. doi:10.1109/JMEMS.2011.2162488

Liu, W., Wang, Z., Wang, G., Zeng, Q., He, W., Liu, L., et al. (2020a). Switched-capacitor-convertors Based on Fractal Design for Output Power Management of Triboelectric Nanogenerator. *Nat. Commun.* 11, 1883. doi:10.1038/s41467-020-15373-y

Liu, Y., Liu, W., Wang, Z., He, W., Tang, Q., Xi, Y., et al. (2020b). Quantifying Contact Status and the Air-Breakdown Model of Charge-Excitation Triboelectric Nanogenerators to Maximize Charge Density. *Nat. Commun.* 11, 1599. doi:10.1038/s41467-020-15368-9

Miki, S., Fujita, T., Kotoge, T., Jiang, Y. G., Uehara, M., Kanda, K., Higuchi, K., and Maenaka, K. (2012). "Electromagnetic Energy Harvester by Using Buried NdFeB," in 2012 IEEE 25th International Conference on Micro Electro Mechanical Systems (MEMS), 1221–1224. doi:10.1109/memsys.2012.6170409

Park, M., Kim, J.-Y., Son, H. J., Lee, C.-H., Jang, S. S., and Ko, M. J. (2016). Low-temperature Solution-Processed Li-Doped SnO2 as an Effective Electron Transporting Layer for High-Performance Flexible and Wearable Perovskite Solar Cells. *Nano Energy* 26, 208–215. doi:10.1016/j.nanoen.2016.04.060

Pu, X., Hu, W., and Wang, Z. L. (2018). Toward Wearable Self-Charging Power Systems: the Integration of Energy-Harvesting and Storage Devices. *Small* 14, 1702817. doi:10.1002/smll.201702817

Qian, J., He, J., Qian, S., Zhang, J., Niu, X., Fan, X., et al. (2020). A Nonmetallic Stretchable Nylon-Modified High Performance Triboelectric Nanogenerator for Energy Harvesting. *Adv. Funct. Mater.* 30, 1907414. doi:10.1002/adfm.201907414

Rome, L. C., Flynn, L., Goldman, E. M., and Yoo, T. D. (2005). Generating Electricity while Walking with Loads. *Science* 309, 1725–1728. doi:10.1126/science.1111063

Saadon, S., and Sidek, O. (2011). A Review of Vibration-Based MEMS Piezoelectric Energy Harvesters. *Energ. Convers. Manage.* 52, 500–504. doi:10.1016/j.enconman.2010.07.024

Safaei, M., Sodano, H. A., and Anton, S. R. (2019). A Review of Energy Harvesting Using Piezoelectric Materials: State-Of-The-Art a Decade Later (2008-2018). *Smart Mater. Struct.* 28, 113001. doi:10.1088/1361-665X/ab36e4

Sang, M., Wang, S., Liu, S., Liu, M., Bai, L., Jiang, W., et al. (2019). A Hydrophobic, Self-Powered, Electromagnetic Shielding PVDF-Based Wearable Device for Human Body Monitoring and protection. *ACS Appl. Mater. Inter.* 11, 47340–47349. doi:10.1021/acsami.9b16120

Sebald, G., Guyomar, D., and Agbossou, A. (2009). On Thermoelectric and Pyroelectric Energy Harvesting. *Smart Mater. Struct.* 18, 125006. doi:10.1088/0964-1726/18/12/125006

Siddique, A. R. M., Mahmud, S., and Heyst, B. V. (2015). A Comprehensive Review on Vibration Based Micro Power Generators Using Electromagnetic and Piezoelectric Transducer Mechanisms. *Energ. Convers. Manage.* 106, 728–747. doi:10.1016/j.enconman.2015.09.071

Siddique, A. R. M., Mahmud, S., and Heyst, B. V. (2017). A Review of the State of the Science on Wearable Thermoelectric Power Generators (TEGs) and Their Existing Challenges. *Renew. Sustain. Energ. Rev.* 73, 730–744. doi:10.1016/j.rser.2017.01.177

Starner, T. (1996). Human-powered Wearable Computing. *IBM Syst. J.* 35, 618–629. doi:10.1147/sj.353.0618

Tang, W., Jiang, T., Fan, F. R., Yu, A. F., Zhang, C., Cao, X., et al. (2015). Liquid-metal Electrode for High-Performance Triboelectric Nanogenerator at an Instantaneous Energy Conversion Efficiency of 70.6%. *Adv. Funct. Mater.* 25, 3718–3725. doi:10.1002/adfm.201501331

Wang, S., Ding, L., Fan, X., Jiang, W., and Gong, X. (2018a). A Liquid Metal-Based Triboelectric Nanogenerator as Stretchable Electronics for Safeguarding and Self-Powered Mechanosensing. *Nano Energy* 53, 863–870. doi:10.1016/j.nanoen.2018.09.035

Wang, S., Gong, L., Shang, Z., Ding, L., Yin, G., Jiang, W., et al. (2018b). Novel Safeguarding Tactile E-Skins for Monitoring Human Motion Based on SST/PDMS-AgNW-PET Hybrid Structures. *Adv. Funct. Mater.* 28, 1707538. doi:10.1002/adfm.201707538

Wang, S., Yuan, F., Liu, S., Zhou, J., Xuan, S., Wang, Y., et al. (2020). A Smart Triboelectric Nanogenerator with Tunable Rheological and Electrical Performance for Self-Powered Multi-Sensors. *J. Mater. Chem. C* 8, 3715–3723. doi:10.1039/C9TC05969E

Wang, Z., Liu, W., Hu, J., He, W., Yang, H., Ling, C., et al. (2020). Two Voltages in Contact-Separation Triboelectric Nanogenerator: From Asymmetry to Symmetry for Maximum Output. *NANO ENERGY* 69, 104452. doi:10.1016/j.nanoen.2020.104452

Wei, S., Hu, H., and He, S. (2013). Modeling and Experimental Investigation of an Impact-Driven Piezoelectric Energy Harvester from Human Motion. *Smart Mater. Struct.* 22, 105020. doi:10.1088/0964-1726/22/10/105020

Wen, Z., Yeh, M.-H., Guo, H., Wang, J., Zi, Y., Xu, W., et al. (2016). Self-powered Textile for Wearable Electronics by Hybridizing Fiber-Shaped Nanogenerators, Solar Cells, and Supercapacitors. *Sci. Adv.* 2, e1600097. doi:10.1126/sciadv.1600097

Xie, J., Li, F., Kuang, S., Yang, H., Li, X., Tang, S., et al. (2020). Modeling and Motion Control of a Liquid Metal Droplet in a Fluidic Channel. *Ieee/asme Trans. Mechatron.* 25, 942–950. doi:10.1109/TMECH.2020.2964387

Xiujian, C., Jie, Z., Shuo, Q., Xushi, N., Jichao, Q., Xiaojuan, H., et al. (2018). All-in-one Filler-Elastomer-Based High-Performance Stretchable Piezoelectric Nanogenerator for Kinetic Energy Harvesting and Self-Powered Motion Monitoring. *Nano Energy* 53, 550. doi:10.1016/j.nanoen.2018.09.006

Yang, B., Lee, C., Wei, L. K., and Lim, S.-P. (2010). Hybrid Energy Harvester Based on Piezoelectric and Electromagnetic Mechanisms. *J. Micro/nanolith. MEMS MOEMS* 9, 023002. doi:10.1117/1.3373516

Yang, W., Chen, J., Zhu, G., Yang, J., Bai, P., Su, Y., et al. (2013). Harvesting Energy from the Natural Vibration of Human Walking. *ACS Nano* 7, 11317–11324. doi:10.1021/nn405175z

Yang, Y., Sun, N., Wen, Z., Cheng, P., Zheng, H., Shao, H., et al. (2018). Liquid-Metal-Based Super-stretchable and Structure-Designable Triboelectric Nanogenerator for Wearable Electronics. *ACS Nano* 12, 2027–2034. doi:10.1021/acsnano.8b00147

Yildirim, T., Ghayesh, M. H., Li, W., and Alici, G. (2017a). A Nonlinearly Broadband Tuneable Energy Harvester. *J. Dynamic Syst. Meas. Control.* 139, 011008. doi:10.1115/1.4034321

Yildirim, T., Ghayesh, M. H., Li, W., and Alici, G. (2017). A Review on Performance Enhancement Techniques for Ambient Vibration Energy Harvesters. *Renew. Sustain. Energ. Rev.* 71, 435–449. doi:10.1016/j.rser.2016.12.073

Yildirim, T., Ghayesh, M. H., Searle, T., Li, W., and Alici, G. (2017b). A Parametrically Broadband Nonlinear Energy Harvester. *J. Energ. Resour. Tech.* 139, 011008. doi:10.1115/1.4034514

Yu, L., Yi, Y., Yao, T., Song, Y., Chen, Y., Li, Q., et al. (2019). All VN-Graphene Architecture Derived Self-Powered Wearable Sensors for Ultrasensitive Health Monitoring. *Nano Res.* 12, 331–338. doi:10.1007/s12274-018-2219-1

Zeng, W., Tao, X.-M., Chen, S., Shang, S., Chan, H. L. W., and Choy, S. H. (2013). Highly Durable All-Fiber Nanogenerator for Mechanical Energy Harvesting. *Energ. Environ. Sci.* 6, 2631–2638. doi:10.1039/c3ee41063c

Zhang, C., Tang, W., Han, C., Fan, F., and Wang, Z. L. (2014). Theoretical Comparison, Equivalent Transformation, and Conjunction Operations of Electromagnetic Induction Generator and Triboelectric Nanogenerator for Harvesting Mechanical Energy. *Adv. Mater.* 26, 3580–3591. doi:10.1002/adma.201400207

Zhang, J., Yan, S., Yuan, D., Alici, G., Nguyen, N.-T., Ebrahimi Warkiani, M., et al. (2016). Fundamentals and Applications of Inertial Microfluidics: a Review. *Lab. Chip* 16, 10–34. doi:10.1039/C5LC01159K

Zheng, L., Lin, Z.-H., Cheng, G., Wu, W., Wen, X., Lee, S., et al. (2014). Silicon-based Hybrid Cell for Harvesting Solar Energy and Raindrop Electrostatic Energy. *Nano Energy* 9, 291–300. doi:10.1016/j.nanoen.2014.07.024

Zhu, H., Li, Y., Shen, W., and Zhu, S. (2019). Mechanical and Energy-Harvesting Model for Electromagnetic Inertial Mass Dampers. *Mech. Syst. Signal Process.* 120, 203–220. doi:10.1016/j.ymssp.2018.10.023

Zi, Y., Guo, H., Wen, Z., Yeh, M.-H., Hu, C., and Wang, Z. L. (2016). Harvesting Low-Frequency (. *ACS Nano* 10, 4797–4805. doi:10.1021/acsnano.6b01569

Zuo, L., Scully, B., Shestani, J., and Zhou, Y. (2010). Design and Characterization of an Electromagnetic Energy Harvester for Vehicle Suspensions. *Smart Mater. Struct.* 19, 045003. doi:10.1088/0964-1726/19/4/045003

Conflict of Interest: The authors declare that the research was conducted in the absence of any commercial or financial relationships that could be construed as a potential conflict of interest.